Charge radii of neutron-deficient ^{36}K and ^{37}K

D. M. Rossi,[1,*] K. Minamisono,[1,2,†] H. B. Asberry,[1,3] G. Bollen,[1,2] B. A. Brown,[1,2] K. Cooper,[1,3] B. Isherwood,[1,2]
P. F. Mantica,[1,3] A. Miller,[1,2] D. J. Morrissey,[1,3] R. Ringle,[1] J. A. Rodriguez,[1] C. A. Ryder,[1] A. Smith,[1]
R. Strum,[1,2] and C. Sumithrarachchi[1]

[1]*National Superconducting Cyclotron Laboratory, Michigan State University, East Lansing, Michigan 48824, USA*
[2]*Department of Physics and Astronomy, Michigan State University, East Lansing, Michigan 48824, USA*
[3]*Department of Chemistry, Michigan State University, East Lansing, Michigan 48824, USA*

Background: The systematic trend in mean-square charge radii as a function of proton or neutron number exhibits a discontinuity at the nucleon-shell closures. While the established $N = 28$ shell closure is evident in the charge radii of the isotopic chains of K through Mn, a similar signature of the $N = 20$ shell closure is absent in the Ca region.

Purpose: The isotope shift between neutron-deficient ^{36}K and ^{37}K was determined to investigate the change of the mean-square charge radii across $N = 20$ in the K isotopic chain.

Methods: The $D1$ atomic hyperfine spectra of ^{36}K and ^{37}K were measured using an optical pumping and subsequent β-decay asymmetry detection technique. Atomic rate equations were solved to fit the resonant line shape. The result was compared to Skyrme energy-density functional and shell-model calculations.

Results: The isotope shift was obtained as $\delta\nu^{37,36} = -139(4)(3)$ MHz. Using a re-evaluated isotope shift, $\delta\nu^{39,37} = -264(2)(3)$ MHz, the isotope shift relative to ^{39}K was determined to be $\delta\nu^{39,36} = -403(5)(4)$ MHz. The differential mean-square charge radius was then deduced as $\delta\langle r^2\rangle^{39,36} = -0.16(5)(8)$ fm^2. The Skyrme energy-density functional and shell-model calculations overpredict the experimental values below $N = 20$ and underpredict them above $N = 20$, and their agreement is marginal.

Conclusions: The absence of the shell-closure signature at $N = 20$ in the K isotopic chain is understood as a balance between the monopole and the quadrupole proton-core polarizations below and above $N = 20$, respectively.

PACS number(s): 21.10.Ft, 21.60.−n, 27.30.+t, 32.80.Xx

I. INTRODUCTION

Nuclear charge radii have been used extensively to systematically characterize the onset of deformation, pairing effects, and the presence of nucleon shell closures [1,2]. The shell closures have been identified by abrupt changes in the slope of the mean-square charge radii as a function of the number of protons or neutrons in the nucleus. While there is a clear discontinuity in the charge radii, for example, at the $N = 28$ neutron-shell closure for the isotopic chains of K through Mn, the signature at $N = 20$ is absent in the Ca region. The mean-square charge radii of the Ar [3,4], K [5–9], and Ca [10–12] isotopic chains vary monotonically across $N = 20$ in contrast to the discontinuity evident at $N = 28$. The absence of an unambiguous signature of the shell effect has been attributed to the cancellation of the monopole and quadrupole proton core polarizations under successive neutron addition [3], but a quantitative description of this phenomenon has not been provided yet.

The hyperfine (HF) spectra of the neutron-deficient ^{36,37}K isotopes were measured using optical pumping and subsequent β-decay asymmetry detection. The isotope shifts of ^{36,37}K were deduced relative to that of the stable ^{39}K and the differential mean-square charge radii were extracted. The

results are compared to Skyrme energy-density functional and shell-model calculations. The absence of a manifestation of the $N = 20$ shell closure in the Ca region is discussed in terms of the aforementioned core-polarization effects.

II. EXPERIMENTAL METHOD

The radioactive ^{36}K ($T_{1/2} = 0.342$ s; $I^\pi = 2^+$) and ^{37}K ($T_{1/2} = 1.226$ s; $I^\pi = 3/2^+$) ion beams were produced by fragmentation of a stable ^{40}Ca beam on a $^{\text{nat}}$Be target. The ^{40}Ca ions were accelerated to 140 MeV/nucleon in the coupled cyclotrons at National Superconducting Cyclotron Laboratory (NSCL) at Michigan State University. The ^{36}K or ^{37}K beams were separated from other fragmentation products in the A1900 fragment separator [13], thermalized in the NSCL gas stopper [14], and extracted as singly charged ions at an energy of 30 keV. The low-energy ion beams were transported to the beam cooling and laser spectroscopy (BECOLA) facility [15], where they were injected into a radio frequency quadrupole (RFQ) cooler [16] filled with helium buffer gas at ∼100 mTorr. The injected ion beams were thermalized through collisions with the buffer gas and extracted at an energy of $29\,856 \pm 2$ eV towards the collinear-laser spectroscopy (CLS) beam line. The bias voltage was measured by a precision high-voltage divider [17]. The uncertainty was resulted from the calibration of the voltage divider and from a possible shift of ion-beam energy from the bias voltage due to imperfect cooling, which was estimated to be less than 1 V.
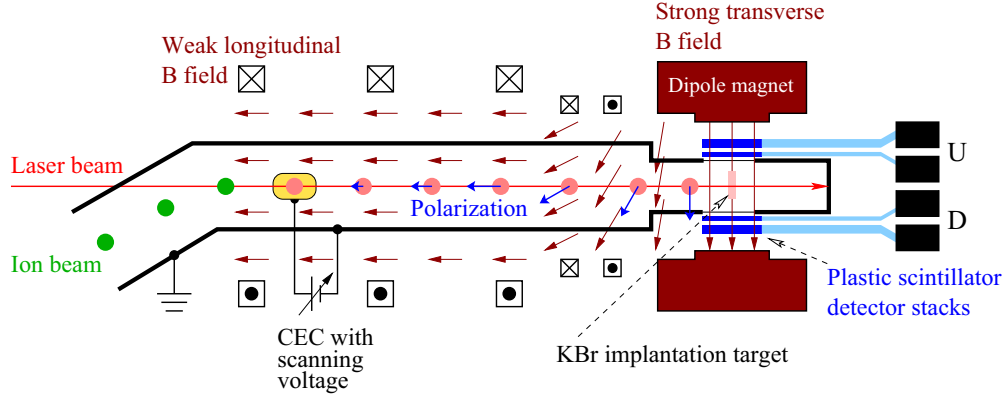
―――――――
*rossi@nscl.msu.edu
†minamiso@nscl.msu.edu

FIG. 1. (Color online) Schematic drawing of the setup for the optical pumping and β-decay asymmetry measurement at the BECOLA facility. The polarization was adiabatically rotated by 90° from the horizontal direction in the CLS beam line to the vertical direction in the dipole magnet.

A continuous-wave 532-nm Spectra Physics diode-pumped solid-state laser was used to pump a Sirah Matisse TS Ti:sapphire ring laser, producing ∼700 mW of 769-nm light with 10 W of pump-laser power for laser spectroscopy on the atomic $D1$ transition ($4s\ ^2S_{1/2} \leftrightarrow 4p\ ^2P_{1/2}$) of ^{36,37}K. The laser light was transported to an optical table close to the CLS beam line using a single-mode, polarization-maintaining optical fiber. The polarization axis of the linearly polarized light was redefined to the vertical orientation using a half-wave ($\lambda/2$) plate and a polarization cube. The laser-light power was adjusted to and stabilized at 20 mW using a laser power controller [18] with a ±0.05% power fluctuation. The diameter and focus of the laser light was adjusted using an optical telescope, with a transmission through the CLS beam line of 87%. Circular polarization of the laser light was produced using a quarter-wave ($\lambda/4$) plate. A retractable $\lambda/2$ plate on a motorized flipper mount located behind the $\lambda/4$ plate was used to switch the helicity of the laser light. The ^{36}K or ^{37}K ion beams were deflected onto the optical axis of the laser light in the CLS beam line, as shown in Fig. 1. A charge-exchange cell (CEC) [19] containing sodium vapor was used to neutralize 50% of the incoming ion beam. The neutral beam rates were approximately 500 and 3000 s^{-1} for ^{36}K and ^{37}K, respectively.

A scanning voltage was applied to the CEC to tune the Doppler-shifted laser frequency into resonance with the HF transitions. The scanning voltage was calibrated using a high precision voltage meter with an accuracy of 0.06%. The typical ripple of the scanning voltage was 0.2 V peak to peak. The laser frequency was set to 13 002.5142 cm^{-1} and 13 002.2844 cm^{-1} for the $D1$ transition of ^{36}K and ^{37}K, respectively. These laser frequencies were chosen to scan the voltage applied to the CEC in a range around zero volts, from −80 to 100 V for ^{36}K and from −40 to 50 V for ^{37}K, to minimize the ion-beam steering effects. A weak longitudinal magnetic field (2×10^{-3} T) was generated using electric coils placed along the CLS beam line, defining the quantization axis of the atomic polarization. A dipole magnet producing a strong transverse magnetic field (0.4 T) was located at the end of the CLS beam line, approximately 2.5 m downstream from the exit of the CEC. Two coils generating a weak transverse field were placed in front of the dipole magnet to achieve a gradual

transition of the magnetic field from longitudinal to transverse direction together with the fringing field of the dipole magnet, facilitating an adiabatic rotation of the polarization by 90°.

The ^{36}K or ^{37}K atoms were implanted into a cubic KBr single crystal placed at the center of the dipole magnet, where the hyperfine interaction was decoupled due to the strong magnetic field. Two sets of thin plastic scintillators (1 and 2 mm in thickness), each optically coupled to a photomultiplier tube by a plastic light guide, were used in coincidence to detect the β^+ particles from the ^{36}K or ^{37}K decay. One set was placed at 0° (D) and the other at 180° (U) with respect to the field direction of the dipole magnet. The total counting rates of β^+ particles were approximately 100 and 600 s^{-1} for ^{36}K and ^{37}K, respectively.

III. HYPERFINE INTERACTION AND OPTICAL PUMPING

A. Hyperfine structure

The shift of an atomic energy level due to the hyperfine interaction relative to an atomic fine level is given by

$$\Delta E = \frac{K}{2}A^{\mathrm{HF}} + \frac{3K(K+1) - 4I(I+1)J(J+1)}{8I(2I-1)J(2J-1)}B^{\mathrm{HF}},$$

(1)

with $K = F(F+1) - I(I+1) - J(J+1)$, where F is the quantum number defined by the vector $\mathbf{F} = \mathbf{I} + \mathbf{J}$ with I and J being the nuclear and atomic spins, respectively. A^{HF} and B^{HF} are the HF coupling constants defined as

$$A^{\mathrm{HF}} = \frac{\mu_I B_e(0)}{IJ},$$

(2)

$$B^{\mathrm{HF}} = eQ_s\left\langle \frac{\partial^2 V_e}{\partial z^2} \right\rangle,$$

(3)

where μ_I is the magnetic dipole moment, $B_e(0)$ is the magnetic field generated by the atomic electrons at the center of the nucleus, e is the electric unit charge, Q_s is the spectroscopic electric-quadrupole moment, and $\langle \partial^2 V_e/\partial z^2 \rangle$ is the electric field gradient produced by the atomic electrons at the center of the nucleus.

While A^{HF} and B^{HF} are associated with the nuclear moments, the hyperfine centroid frequency contains information

on the nuclear charge radius. The isotope shift is defined as the difference between the centroid frequencies of two isotopes A and A' of an element and is given by

$$\delta \nu^{A,A'} = \nu^{A'} - \nu^A = M \frac{m_{A'} - m_A}{m_A m_{A'}} + F \delta \langle r^2 \rangle^{A,A'}, \quad (4)$$

where M and F are the mass and field shift coefficients, respectively, m is the atomic mass, and $\delta \langle r^2 \rangle^{A,A'}$ is the differential mean-square charge radius between the A and A' isotopes. The mass coefficient is defined as $M = k_{\mathrm{NMS}} + k_{\mathrm{SMS}}$ with $k_{\mathrm{NMS}} = \nu m_e$, where k_{NMS} and k_{SMS} are the normal and specific mass shift coefficients, respectively, ν is the transition frequency, and m_e is the electron mass.

The atomic Zeeman splitting must be taken into account in the presence of a magnetic field, which breaks the degeneracy of each F state, producing $(2F + 1)$ substates. Since the $D1$ atomic transition used in the present experiment involved two states with $J = 1/2$, the Breit-Rabi formula [20,21] was used to determine the energy shift $\Delta E_{F=I\pm 1/2}$ of each m_F substate with respect to the fine-structure energy:

$$\frac{\Delta E_{F=I\pm 1/2}}{\Delta E_{\mathrm{HF}}} = -\frac{1}{2(2I+1)} \pm \frac{1}{2}\sqrt{1 + \frac{4m_F}{2I+1}e_f + e_f^2}, \quad (5)$$

$$e_f = \frac{g_J \mu_B B_w}{\Delta E_{\mathrm{HF}}}, \quad (6)$$

$$g_J = 1 + \frac{J(J+1) + S(S+1) - L(L+1)}{2J(J+1)}, \quad (7)$$

where e_f is the Zeeman energy measured in units of ΔE_{HF}, which is the HF splitting between the $F = I - 1/2$ and $F = I + 1/2$ states at zero field, g_J is the Landé g factor with J, S, and L the total angular, spin, and orbital atomic quantum numbers, respectively, μ_B is the Bohr magneton, and B_w is the magnetic field strength.

B. Nuclear polarization and β-decay asymmetry

An optical-pumping technique [22,23] was used to polarize ^{36,37}K. Circularly polarized light with positive σ^+ and negative σ^- helicities was used to drive transitions between m_F substates with $\Delta m_F = +1$ and $\Delta m_F = -1$, respectively. Each atom can undergo several electronic excitation and de-excitation cycles as it passes through the interaction region, leading to a redistribution of the population in the m_F substates. The optical pumping occurs in the weak magnetic field, where the quantum state of the atom is well defined by $|F, m_F\rangle$. In the strong magnetic field, on the other hand, the nuclear and electron spins become good quantum numbers separately (Paschen-Back regime), leading to a quantum state described by $|m_I, m_J\rangle$. The variation of HF-energy levels as a function of an external magnetic field is shown in Fig. 2. The nuclear polarization P_I is given by

$$P_I = \frac{\langle m_I \rangle}{I} = \frac{\sum_m m \, p_m}{I}, \quad (8)$$

where $\sum_m p_m = 1$, m runs from $-I$ to I, and p_m is the population of the mth substate.
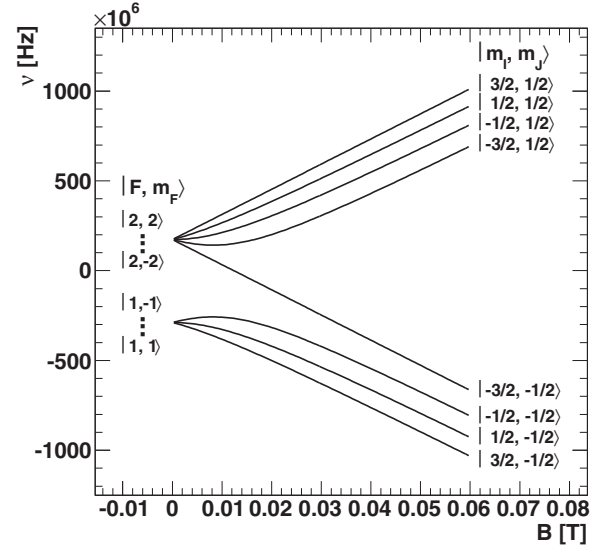

FIG. 2. Magnetic-field dependence of the m_F substates. The ground-state HF structure of ^{39}K is shown as an example.

β decay with a nonzero nuclear polarization leads to an asymmetric angular distribution $N_\beta(\vartheta)$ [24] given by

$$N_\beta(\vartheta) = 1 + \left(\frac{v}{c}\right) A_\beta P_I \cos \vartheta, \quad (9)$$

where ϑ is the emission angle with respect to the polarization direction, v is the velocity of the β particle, c is the velocity of light, and A_β is the β-decay asymmetry parameter. The average β^+ energy is large for both ^{36}K and ^{37}K so that $v/c \to 1$, and by using Eq. (9) the U/D counting rate ratio is given by

$$U/D = G \frac{N_\beta(\pi)}{N_\beta(0)} = G \frac{1 - A_\beta P_I}{1 + A_\beta P_I}, \quad (10)$$

where G is a geometrical factor related to small differences in the detection efficiencies and solid angles between the U and D detectors.

HF structure measurements using the β-decay asymmetry detection have been performed previously on Mg isotopes and discussed elsewhere [25–27].

C. Rate equation for optical pumping

An algorithm similar to that discussed in Ref. [26] was developed based on the atomic rate equations for optical pumping. The atomic rate equations for each atomic level are a set of first-order differential equations:

$$\frac{dN_i}{dt} = \sum_j P_{ij}^{\uparrow\downarrow}(\nu)(M_j - N_i) + \sum_j P_{ij}^{\downarrow} M_j$$

$$\frac{dM_j}{dt} = \sum_i P_{ij}^{\uparrow\downarrow}(\nu)(-M_j + N_i) - \sum_i P_{ij}^{\downarrow} M_j, \quad (11)$$

where N_i and M_j are the populations of the atomic ground and excited m_F substates, respectively, and $P_{ij}^{\uparrow\downarrow}(\nu)$ and $P_{ij}^{\downarrow}$ are the stimulated and spontaneous decay transition probabilities, respectively, connecting the lower i and upper j levels.

The system of atomic rate equations was included in a χ^2 minimization algorithm to fit the U/D HF spectra of ^{36,37}K. For each minimization step, the differential equations of Eq. (11) were solved numerically for every experimental data point using a fourth order Runge-Kutta algorithm, yielding the population for each m_F level, from which the nuclear polarization and the U/D ratio were calculated according to Eqs. (8) and (10).

IV. RESULTS

The HF spectra for ^{36}K and ^{37}K from the present work are shown in Fig. 3. Two sets of measurements were performed for each isotope with σ^+ and σ^- laser helicities, which are shown in the figure (solid and open circles, respectively) together with their best fits (solid lines). The obtained spectra are asymmetric with respect to the two laser helicities. The asymmetry can be attributed to the asymmetric mapping of the m_I over the m_F substates between the Breit-Rabi and Paschen-Back regimes, as depicted in Fig. 2. A reversal of the sign of the resonance signal can be seen for two adjacent HF transitions in the ^{37}K spectrum measured with σ^-. This reversal can be explained by an elliptical polarization of the laser light (admixture of opposite helicity), mainly caused by the vacuum window into

FIG. 3. (Color online) Hyperfine U/D ratio spectra for ^{36}K (upper panel) and ^{37}K (lower panel). The dashed green vertical lines indicate the centroid frequencies.

the CLS beam line. The sign of the resonance peaks for a given laser helicity changes between ^{36}K and ^{37}K, due to opposite signs of their β-decay asymmetry parameters. The sign of the magnetic moments are known to be positive [21,28]. The sign of the β-decay asymmetry parameter of ^{36}K can be deduced to be $A_\beta(^{36}$K$) > 0$, given the asymmetry parameter for the main decay branch of ^{37}K of $A_\beta(^{37}$K$) = -0.5739$ [29].

A simultaneous fit was performed for the set of spectra measured with σ^+ and σ^-. The relative intensities of the HF transitions were determined by the rate equations, and the overall amplitude was fitted to the data. The overall amplitude parameter took depolarization effects into account, which were due, for example, to the incomplete adiabatic rotation of the nuclear spin during the transition from the weak to the strong magnetic fields, the depolarization during the implantation into the KBr crystal, and a finite polarization relaxation time. The ion beam was steered by the scanning voltage applied to the CEC, resulting in a small misalignment between the outgoing atom beam and laser light. This steering effect was taken into account in the fit. The interaction length between the atom beam and the laser light was assumed to be linearly dependent on the voltage applied to the CEC (and therefore on the laser frequency). The small steering of the ion beam also resulted in a voltage-dependent geometrical factor [Eq. (10)], which was included as a linear function of the frequency in the fit. The HF coupling constants were fixed in the fitting procedure. The $A^{HF}(^2S_{1/2})$ for ^{37}K is known [21]. The $A^{HF}(^2P_{1/2})$ of ^{37}K and those for the $^2S_{1/2}$ and $^2P_{1/2}$ states in ^{36}K have not been measured yet and were evaluated relative to the known coupling constants of ^{39}K [30,31] using known I and μ_I for ^{36,37,39}K [5,21,28], and the relation derived from Eq. (2),

$$A^{HF} = A^{HF}_{ref} \frac{\mu_I}{\mu_{I,ref}} \frac{I_{ref}}{I}. \tag{12}$$

The centroid frequencies of $-373(4)(3)$ MHz and $-233(2)(1)$ MHz relative to a common frequency of 389 286 058.716 MHz were determined from the ^{36}K and ^{37}K data, respectively, where the numbers in the first and second parentheses represent statistical and systematic errors, respectively. The systematic error is dominated by the long-term drift of the high-voltage system that determined the ion-beam energy. The isotope shift is then determined to be $\delta\nu^{37,36} = -139(4)(3)$ MHz. The isotope shift of ^{36}K with respect to ^{39}K required a re-evaluation of $\delta\nu^{39,37}$ using our recent CLS measurement and a previous measurement. The isotope shift of $\delta\nu^{39,37} = -264(3)(3)$ MHz [9] was combined with the value of Behr *et al.* [6] of $\delta\nu^{39,37} = -265(4)$ MHz, leading to a value of $\delta\nu^{39,37} = -264(2)(3)$ MHz. The isotope shift between ^{39}K and ^{36}K was obtained as $\delta\nu^{39,36} = -403(5)(4)$ MHz. The results are listed in Table I. The differential mean-square charge radii were deduced using Eq. (4), the atomic masses from Ref. [33], and the mass and field-shift coefficients of Mårtensson-Pendrill *et al.* [34]. The field-shift coefficient was calculated to be $F = -110(3)$ MHz/fm^2. The specific mass-shift coefficient was found to be $k_{SMS} = -15.3(3.8)$ GHz u, using F and the absolute charge radius of ^{39}K determined by the measurement of x-ray emission in muonic atoms [35]. The resulting total mass shift coefficient $M = 198.2(3.8)$ GHz u leads to
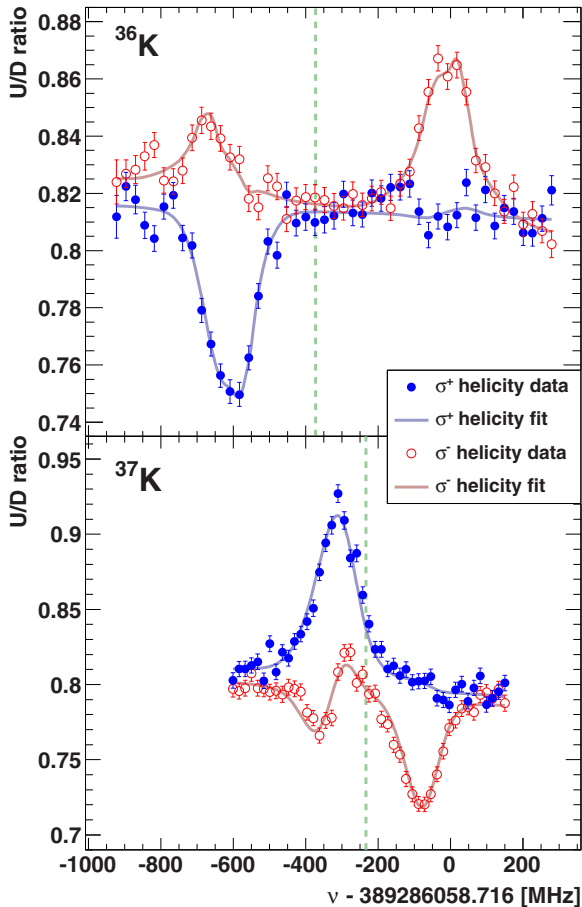
TABLE I. Isotope shifts and differential mean-square charge radii of K isotopes. The statistical and systematic errors are shown in the first and second sets of parentheses, respectively.

A	N	$\delta\nu^{37,A}$ (MHz)	$\delta\nu^{39,A}$ (MHz)	$\delta\langle r^2\rangle^{39,A}$ (fm^2)
36	17	$-139(4)(3)$	$-403(5)(4)$	$-0.16(5)(8)$
37	18	0	$-264(2)(3)^a$	$-0.08(2)(6)$
38	19		$-123.4(1.0)^b$	$-0.089(9)(23)$
39	20		0	0
40	21		$125.6(3)^c$	$0.016(2)(22)$
41	22		$235.3(3)^d$	$0.117(3)(43)$
42	23		$351.2(1.3)^e$	$0.111(12)(63)$
43	24		$459.0(1.2)^c$	$0.129(11)(83)$
44	25		$564.8(1.1)^e$	$0.122(10)(101)$
45	26		$661.7(1.6)^c$	$0.151(15)(118)$
46	27		$764.2(1.2)^e$	$0.092(10)(135)$
47	28		$857.5(1.7)^c$	$0.079(15)(151)$
48	29		$925.8(1.8)^f$	$0.264(16)(167)$
49	30		$992.8(1.8)^f$	$0.420(16)(181)$
50	31		$1064.0(1.9)^f$	$0.513(17)(196)$
51	32		$1131(2)^f$	$0.62(2)(21)$

^{a}Weighted average from Refs. [6] and [9].
^{b}Reference [7].
^{c}Reference [5].
^{d}Weighted average from Refs. [32] and [5].
^{e}Weighted average from Refs. [5] and [8].
^{f}Value calculated using $\delta\nu^{47,A}$ [8] and $\delta\nu^{39,47}$ [5].

a mean-square charge radius of ^{36}K of $\delta\langle r^2\rangle^{39,36} = -0.16 \pm (0.05)_{\text{stat}} \pm (0.08)_{\text{syst}}$ fm^2. The systematic error is dominated by the uncertainties on the mass and field-shift parameters. The mean-square charge radii of the other K isotopes with a known isotope shift relative to ^{39}K were obtained using the same F and M coefficients and are listed in Table I with their respective statistical and systematic errors, which are also dominated by the uncertainties on the mass and field-shift parameters.

V. DISCUSSION

A. Charge radii of the K isotopes

Results of theoretical calculations for differential mean-square charge radii of K and Ca isotopic chains are shown in the lower and upper part of Fig. 4, respectively, where the simplest possible orbital occupations are used. The filling order is $0d_{3/2}$ for $N = 16$–20, $0f_{7/2}$ for $N = 21$–28, and $1p_{3/2}$ for $N = 29$–32. In the harmonic-oscillator (HO) model the point-proton radii are constant. The decreasing trend of the charge radii from $N = 20$ to $N = 28$, shown as the dot-dot-dashed line for Ca is due to the finite charge size of the neutron and relativistic spin-orbit corrections for neutrons [36]. A mass dependence of $A^{-1/12}$ for the oscillator length parameter can reconcile the decreasing trend as shown by the dashed line.

The violet and orange curves show the results of energy-density functional (EDF) calculations carried out for 12 Skyrme forces described by Brown and Schwenk [37] with the simple orbital occupations. The Skyrme forces form two groups, depending on the power σ of the density dependence, which is correlated with the nuclear matter effective mass

m^*/m. The group with $m^*/m \approx 0.7$–0.8 (violet curves) includes the KDE0v1, NRAPR, SKRA, SQMC750, SLy4, and SkM* Skyrme parametrizations, while the group with $m^*/m \approx 1.0$ (orange curves) includes the Ska25, Ska35, SkT1, SkT2, SkT3, and SV-sym32 parametrizations. The Skyrme parameters were determined from fitting nuclear properties of the doubly magic nuclei ^{16,24}O, ^{34}Si, ^{40,48}Ca, ^{58,68}Ni, ^{88}Sr, ^{100,132}Sn, and ^{208}Pb. These properties included binding energies, single-particle energies, mean-square charge radii and mean-square neutron radii. The EDF calculations therefore are expected to describe the mean-square charge radii in the vicinity of the doubly magic ^{40,48}Ca isotopes to within about 0.02 fm. The results of a relativistic mean-field (RMF) calculation with the DD-ME2 interaction [38,39] are also shown as the dot-dashed lines. The RMF approach includes a built-in spin-orbit interaction, a key requirement for the successful description of the discontinuity in the charge radii of the Pb isotopes [40]. The nonrelativistic MF calculation, on the other hand, employs a phenomenological two-body spin-orbit term in the Skyrme force adjusted to experimental data.

The mean-square charge radii for the EDF calculations show discontinuities as a negative curvature at $N = 20$ and a positive curvature at $N = 28$. The curvatures can be traced to the saturation properties of nuclear matter. When approaching $N = 20$ from the neutron-deficient side, neutrons fill the sd shell orbitals, which are already mostly occupied. The nucleus (both protons and neutrons) must expand to maintain a relatively constant interior matter density. Beyond $N = 20$, the neutrons fill the $0f_{7/2}$ orbital of the next major shell ($1p-0f$). Since the $N = 20$ shell gap originates from the closure of a complete LS shell, additional neutrons do not significantly alter the matter density of the core. The charge radii are therefore not affected significantly and remain approximately constant. Beyond $N = 28$, neutrons start to fill the $1p_{3/2}$ orbital. The interior node of this orbital again contributes to the central density, resulting in a self-consistent expansion of the core in order to maintain a constant interior matter density.

The experimental differential mean-square charge radii relative to ^{39}K (listed in Table I) are shown in the bottom part of Fig. 5. The present result for ^{36}K is shown by the solid red circle, together with known data shown by the open black circles. The green band indicates the systematic error associated with the uncertainties in the evaluation of the specific mass-shift coefficient, which dominates the systematic error, and on the calculation of the field-shift coefficient. The top part of Fig. 5 shows the differential mean-square charge radii of the Ca isotopes [41]. The present mean-square charge radius of ^{36}K, and that of ^{37}K with the reduced uncertainty, show a monotonic variation of the mean-square charge radii when crossing $N = 20$. Odd-even staggering is also evident, which is consistent with the trend of the mean-square charge radii in the Ca region around $N = 20$.

Caurier et al. [42] have shown that the increase in the mean-square radii for $^{42-46}$Ca can be explained in the oscillator model when the orbital occupancies are taken from large-basis configuration-interaction (CI) calculations that allow for protons to be excited from the $1s_{1/2}$ and $0d_{3/2}$ orbitals into the $0f_{7/2}$ and $1p_{3/2}$ orbitals with the ZBM2 Hamiltonian [42]. The results for HO and Skyrme calculations with the orbital
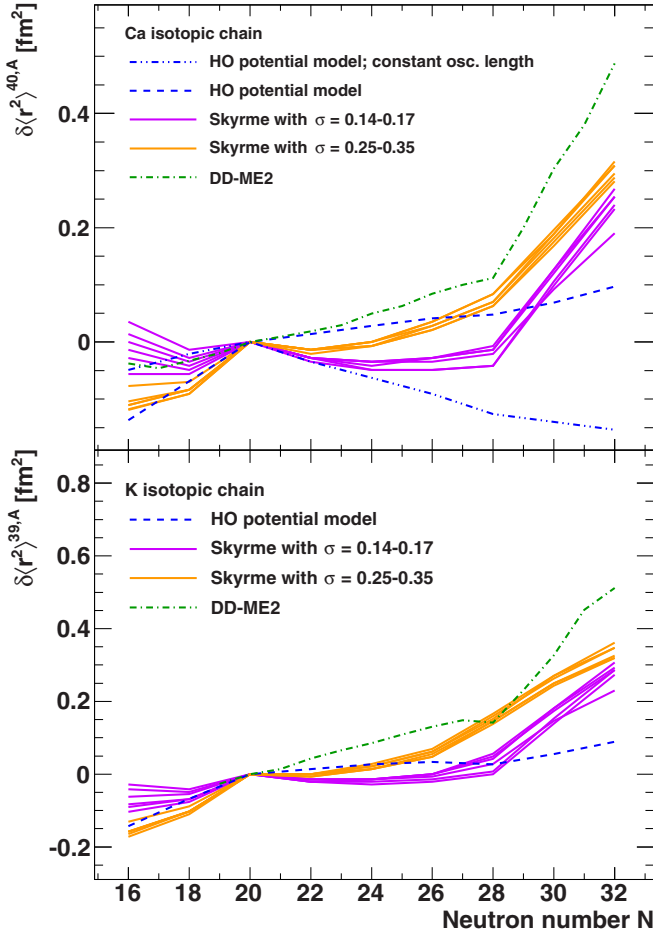
FIG. 4. (Color online) Theoretical differential mean-square charge radii of the Ca (top) and K (bottom) isotopes for the HO potential model with a constant oscillator length (blue dot-dot-dashed line), the adjusted HO potential model (blue dashed line), Skyrme energy-density functional (solid violet and orange lines), and DD-ME2 relativistic mean-field (green dot-dashed line) calculations. The orbital occupations were from the simplified filling approximation described in Sec. V A.
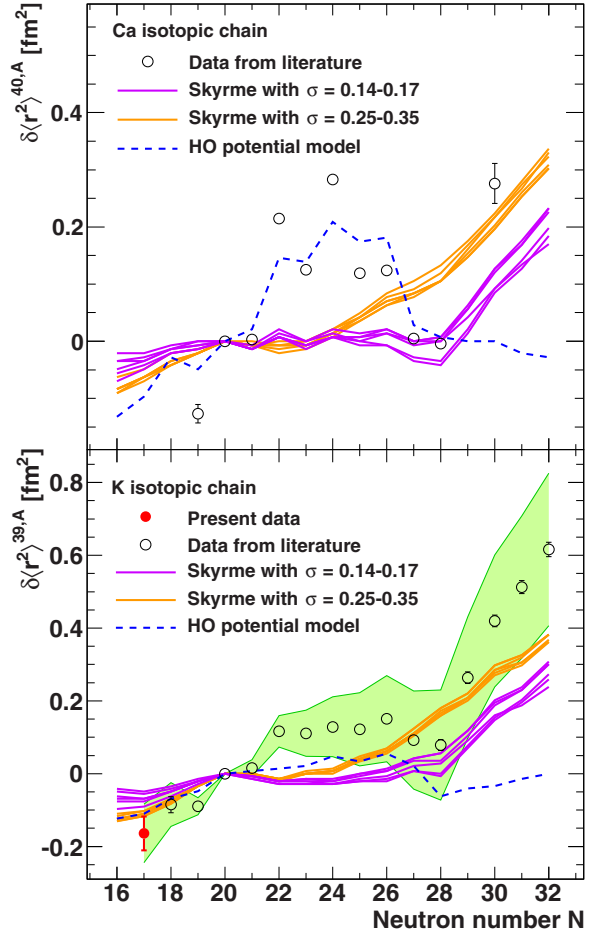
FIG. 5. (Color online) Differential mean-square charge radii of the Ca (top) and K (bottom) isotopes. The solid and dashed lines are the Skyrme and harmonic-oscillator potential calculations, respectively. The orbital occupations were from the shell-model calculation with the ZBM2 (modified) Hamiltonian.

occupancies constrained to CI calculations based on the ZBM2 (modified) Hamiltonian [7] are shown in Fig. 5. The shell-model calculations were carried out with NuShellX [43]. The shell-model calculations in the HO basis as shown by the dashed line reproduce the Ca mean-square charge radii, but the increase of the radii is almost entirely absent in the Skyrme EDF calculations as shown by the violet and orange curves. The flat N dependence of the mean-square charge radii comes from the self-consistent adjustment of the matter density required to keep the interior density approximately constant. The same shell-model calculation for the mean-square charge radii of the K isotopes shows a similar trend except that the theoretical results underestimate the data. Although the ZBM2 calculations describe values of the $E2$-transition strength $B(E2)$ [42], effective charges must be used that originate from proton excitations including $2\hbar\omega$ excitations, which are outside the ZBM2 model space. It is likely that these excitations have to be explicitly included to describe the mean-square charge radii.

The alternative model to explain the increase of the charge radii of ^{42,44,46}Ca is based upon zero-point motion corrections that are connected to the strong $B(E2)$ values observed to the lowest 2^+ states in these nuclei. An estimate for the size of the zero-point motion contribution can be made with the deformed incompressible droplet model with a radius given by

$$R(\theta) = R_0\{1 + \beta_2 Y_{20}(\theta)\}, \tag{13}$$

where β_2 is the quadrupole deformation parameter and Y_{20} is the quadrupole deformation term of spherical harmonics. The variation of the mean-square charge radius is then obtained as

$$\delta\langle r^2 \rangle = \frac{5}{4\pi}\langle r_0^2 \rangle \beta_2^2. \tag{14}$$

The transition strength is given by

$$B(E2 \uparrow) = \left(\frac{5}{4\pi}eZ\langle r_0^2 \rangle\right)^2 \beta_2^2, \tag{15}$$

with Z being the proton number, and therefore a nonzero $B(E2)$ implies a radius increase of

$$\delta\langle r^2 \rangle = \frac{B(E2 \uparrow)}{(5/4\pi)\langle r_0^2 \rangle (eZ)^2}. \tag{16}$$

The experimental $B(E2 \uparrow)$ for ^{42,44,46,50}Ca [44] are 420(30), 473(20), 178(13), and 37(2) e^2 fm^4 giving $\delta\langle r^2 \rangle$ of 0.22(2), 0.25(1), 0.09(1), and 0.020(1) fm^2, respectively. This simple model accounts for the observed increase for ^{42,44,46}Ca, but not for ^{50}Ca. Uher and Sorensen [45] have derived a similar expression for intrinsic vibrations where $B(E2 \uparrow)$ is replaced by $\Sigma_k B(E2, 0^+ \rightarrow 2_k^+)$, where the sum is over low-lying vibrational states. Higher multiples can also be considered [46,47]. Estimation of the size of the zero-point motion contribution to the charge radii of even-even Ca isotopes is possible because the β_2 value can be determined from the $B(E2)$ value of a single 2^+ state. It would be useful to find a method that could be used for the odd-even and odd-odd Ca and K isotopes.

B. Curvature of the charge radii around $N = 20$

The kink strength $S_Z(N)$ [48] was introduced to quantify the monotonic increase of the mean-square charge radii across $N = 20$ and $N = 28$. $S_Z(N)$ is the second differential, or curvature, of the change of the mean-square charge radii and is defined as

$$S_Z(N) = \frac{d^2 R(N)}{d(2N)^2} A^{2/3}, \tag{17}$$

where R is the charge radius. The $A^{2/3}$ term accounts for the mass dependence. The charge radii R were calculated with

$$R_A = \sqrt{R_{A_{\text{ref}}}^2 + \delta\langle r^2 \rangle^{A_{\text{ref}}, A}}, \tag{18}$$

where $R_{A_{\text{ref}}} = R_{39} = 3.4349$ fm was used for the K isotopic chain [41]. The effect of odd-even staggering [49] is eliminated by taking $dN = 2$, leading to $S_Z(N) = [R(N + 2) - 2R(N) + R(N - 2)]A^{2/3}$. However, this leads to the loss of S_Z values for the first and last two isotopes of a given isotopic chain. The present measurement of the charge radius of ^{36}K therefore allows a kink strength value below $N = 20$ to be determined for the first time for the K isotopic chain.

The S_Z values for K are shown in Fig. 6, where the theoretical curves use the same color code as in Fig. 5. The S_Z values for the Ar and Ca isotopes are also shown in the top part of Fig. 6. While the $N = 28$ shell closure is clearly seen as a large positive peak in the K and Ca isotopic chains, no such indication is visible at $N = 20$ for the K and Ar isotopes. The negative S_Z values of the theoretical data for K around $N = 20$ are a consequence of the different monopole proton-core polarization effects for the filling of the sd and $0f_{7/2}$ orbitals, as described in Sec. V A. The small S_Z values for $^{38-41}$K ($19 \leqslant N \leqslant 21$) confirm the linear behavior of the mean-square charge radius variation across $N = 20$, which is not reproduced by the theoretical calculations.

The large positive value observed in experiment at $N = 28$ is not well reproduced by any of the calculations. This problem
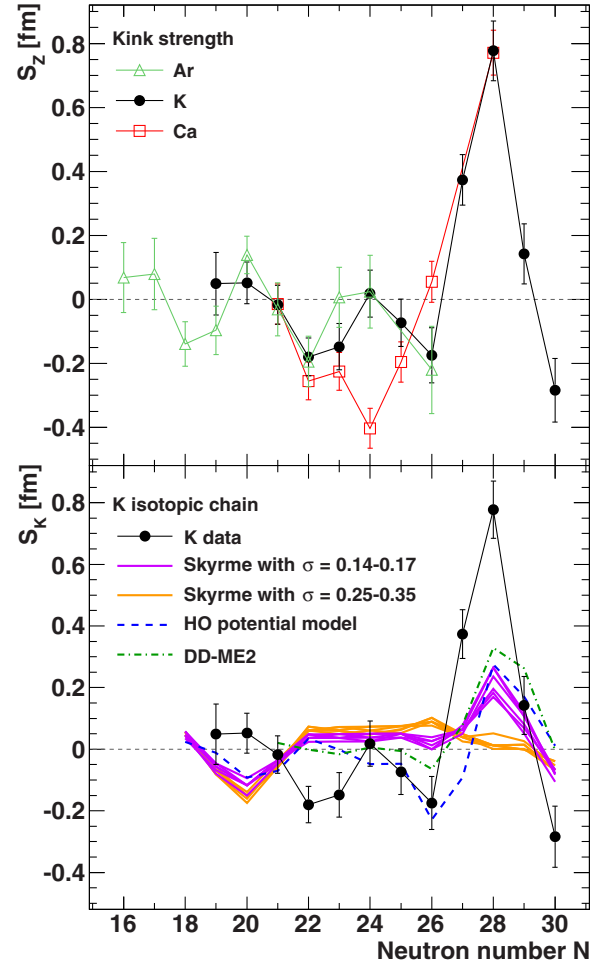

FIG. 6. (Color online) Top: the kink strength trends for the Ar, K, and Ca isotopes. Bottom: the kink strength trend for the K isotopes, for both the experimental data and the calculations.

is similar to that observed in recent EDF calculations for the lead isotopes above $N = 126$ (see Fig. 5 in Ref. [50]).

The behavior of the experimental S_Z values for $20 \leqslant N \leqslant 28$ is similar for both K and Ca isotopes. While the theoretical S_Z curves for K are mostly flat and therefore do not present a significant curvature of the mean-square charge radii in this region, the experimental K and Ca mean-square charge radii show a parabolic trend resulting in a negative curvature. This behavior is especially striking in the Ca isotopic chain, where ^{40}Ca and ^{48}Ca have approximately the same charge radii, which is attributed to quadrupole core-polarization effects [45], and has been discussed previously for the Ar isotopes [3,4]. The amplitude of the parabola for the K isotopes is smaller than that of Ca, but the negative curvature is not reproduced by theory.

The experimental mean-square charge radii of the K and Ca isotopes below $N = 20$ are overpredicted by the Skyrme EDF calculations. Since these calculations only show a weak quadrupole proton-core polarization effect, the variation of the experimental charge radii below $N = 20$ is dominated by the monopole proton-core polarization as opposed to the variation above $N = 20$, where the quadrupole proton-core polarization takes precedence. The disappearance of the shell effect in the

charge radii at $N = 20$ is the result of a subtle balance between the variation of the mean-square charge radii dominated by the monopole proton-core polarization below $N = 20$ and the onset of the quadrupole proton-core polarization above $N = 20$. Although the proton-core polarization and the odd-even staggering effects are strongly dependent on Z, the monotonic increase of the mean-square charge radii across $N = 20$ persists in the Ca region. The reason for this common behavior of the monotonic variation, at least among the Ar, K, and Ca isotopes, remains an open question. The extension of charge radius measurements of K and Ca isotopes deep into the sd shell is important for the quantitative understanding of the shell effects. It is also noted that the Sc charge radii show a monotonically decreasing trend with successive addition of neutrons into the $0f_{7/2}$ orbital [51], in contrast to the parabolic shape seen in the Ca isotopes. The similar decreasing trend can be seen up to the Mn isotopes [52]. Experimental studies of the Sc charge radii across $N = 20$ are also important to provide insight into the global description of the disappearance of shell effects at $N = 20$.

VI. CONCLUSIONS

The $D1$ hyperfine spectra of ^{36}K and ^{37}K were measured using optical pumping and subsequent β-decay asymmetry detection at the BECOLA facility at NSCL. The β-decay asymmetry was detected as a function of the scanning voltage applied to the CEC to tune the Doppler-shifted laser frequency into resonance. Atomic rate equations were solved within the fitting procedure to the measured resonance spectra, from which the centroid frequencies were extracted. The mean-square charge radius of ^{36}K was determined as $\delta\langle r^2\rangle^{39,36} = -0.16(5)(8)$ fm^2, together with the reanalyzed mean-square charge radius of ^{37}K of $\delta\langle r^2\rangle^{39,37} = -0.08(2)(6)$ fm^2.

The extracted mean-square charge radii of ^{36,37}K were compared to Skyrme EDF and shell-model calculations together with the other K isotopes. The overall agreement is marginal and the theories overpredict the mean-square charge radii below and underpredict them above the $N = 20$ neutron-shell closure. All predicted mean-square charge radii show a discontinuity at $N = 20$, while such a signature is absent in the experimental data. This absence is attributed to a balance between the variation of the mean-square charge radii below $N = 20$, dominated by the monopole proton-core polarization, and the onset of deformation above $N = 20$, accounted for by the quadrupole proton-core polarization. The monotonic increase of the mean-square charge radii across $N = 20$ persists in the Ca region regardless of Z. The reason for this common variation across $N = 20$, at least among the Ar, K, and Ca isotopes, remains an open question. Additional measurements of charge radii in the Ca region are important for the understanding of the evolution of the shell-effect signature at $N = 20$, and for the underlying interplay between the monopole and quadrupole core-polarization effects.

[1] B. Cheal and K. T. Flanagan, J. Phys. G: Nucl. Part. Phys. **37**, 113101 (2010).

[2] K. Blaum, J. Dilling, and W. Nörtershäuser, Phys. Scr. **T152**, 014017 (2013).

[3] A. Klein, B. Brown, U. Georg, M. Keim, P. Lievens, R. Neugart, M. Neuroth, R. Silverans, L. Vermeeren, and I. Collaboration, Nucl. Phys. A **607**, 1 (1996).

[4] K. Blaum, W. Geithner, J. Lassen, P. Lievens, K. Marinova, and R. Neugart, Nucl. Phys. A **799**, 30 (2008).

[5] F. Touchard, P. Guimbal, S. Büttgenbach, R. Klapisch, M. De Saint Simon, J. M. Serre, C. Thibault, H. T. Duong, P. Juncar, S. Liberman, J. Pinard, and J. L. Vialle, Phys. Lett. B **108**, 169 (1982).

[6] J. A. Behr, A. Gorelov, T. Swanson, O. Häusser, K. P. Jackson, M. Trinczek, U. Giesen, J. M. D'Auria, R. Hardy, T. Wilson, P. Choboter, F. Leblond, L. Buchmann, M. Dombsky, C. D. P. Levy, G. Roy, B. A. Brown, and J. Dilling, Phys. Rev. Lett. **79**, 375 (1997).

[7] M. L. Bissell, J. Papuga, H. Naïdja, K. Kreim, K. Blaum, M. De Rydt, R. F. Garcia Ruiz, H. Heylen, M. Kowalska, R. Neugart, G. Neyens, W. Nörtershäuser, F. Nowacki, M. M. Rajabali, R. Sanchez, K. Sieja, and D. T. Yordanov, Phys. Rev. Lett. **113**, 052502 (2014).

[8] K. Kreim, M. L. Bissell, J. Papuga, K. Blaum, M. D. Rydt, R. F. G. Ruiz, S. Goriely, H. Heylen, M. Kowalska, R. Neugart, G. Neyens, W. Nörtershäuser, M. M. Rajabali, R. S. Alarcon, H. H. Stroke, and D. T. Yordanov, Phys. Lett. B **731**, 97 (2014).

[9] D. M. Rossi, K. Minamisono, B. R. Barquest, G. Bollen, K. Cooper, M. Davis, K. Hammerton, M. Hughes, P. F. Mantica, D. J. Morrissey, R. Ringle, J. A. Rodriguez, C. A. Ryder, S. Schwarz, R. Strum, C. Sumithrarachchi, D. Tarazona, and S. Zhao, Rev. Sci. Instrum. **85**, 093503 (2014).

[10] A. Andl, K. Bekk, S. Göring, A. Hanser, G. Nowicki, H. Rebel, G. Schatz, and R. C. Thompson, Phys. Rev. C **26**, 2194 (1982).

[11] L. Vermeeren, R. E. Silverans, P. Lievens, A. Klein, R. Neugart, C. Schulz, and F. Buchinger, Phys. Rev. Lett. **68**, 1679 (1992).

[12] L. Vermeeren, P. Lievens, R. E. Silverans, U. Georg, M. Keim, A. Klein, R. Neugart, M. Neuroth, and F. Buchinger (the ISOLDE Collaboration), J. Phys. G: Nucl. Part. Phys. **22**, 1517 (1996).

[13] D. J. Morrissey, B. M. Sherrill, M. Steiner, A. Stolz, and I. Wiedenhoever, *14th International Conference on Electromagnetic Isotope Separators and Techniques Related to their Applications*, Nucl. Instrum. Methods Phys. Res. B **204**, 90 (2003).

[14] K. Cooper, C. Sumithrarachchi, D. Morrissey, A. Levand, J. Rodriguez, G. Savard, S. Schwarz, and B. Zabransky, Nucl. Instrum. Methods Phys. Res. A **763**, 543 (2014).

[15] K. Minamisono, P. F. Mantica, A. Klose, S. Vinnikova, A. Schneider, B. Johnson, and B. R. Barquest, Nucl. Instrum. Methods Phys. Res. A **709**, 85 (2013).

[16] B. R. Barquest, Ph.D. thesis, Michigan State University, 2014.

[17] Ohm Labs Inc., high-voltage divider, http://www.ohm-labs.com/index.html

[18] Brockton Electro-optics Corp., laser power controller, http://www.brocktoneo.com

[19] A. Klose, K. Minamisono, C. Geppert, N. Frömmgen, M. Hammen, J. Krämer, A. Krieger, C. D. P. Levy, P. F. Mantica, W. Nörtershäuser, and S. Vinnikova, Nucl. Instrum. Methods Phys. Res. A **678**, 114 (2012).

[20] G. Breit and I. I. Rabi, Phys. Rev. **38**, 2082 (1931).

[21] C. von Platen, J. Bonn, U. Köpf, R. Neugart, and E.-W. Otten, Z. Phys. **244**, 44 (1971).

[22] E. Arnold, J. Bonn, R. Gegenwart, W. Neu, R. Neugart, E. W. Otten, G. Ulm, and K. Wendt (the ISOLDE Collaboration), Phys. Lett. B **197**, 311 (1987).

[23] M. Keim, U. Georg, A. Klein, R. Neugart, M. Neuroth, S. Wilbert, P. Lievens, L. Vermeeren, and B. A. Brown (the ISOLDE Collaboration), Eur. Phys. J. A **8**, 31 (2000).

[24] J. D. Jackson, S. B. Treiman, and H. W. Wyld, Phys. Rev. **106**, 517 (1957).

[25] D. T. Yordanov, M. Kowalska, K. Blaum, M. De Rydt, K. T. Flanagan, P. Lievens, R. Neugart, G. Neyens, and H. H. Stroke, Phys. Rev. Lett. **99**, 212501 (2007).

[26] M. Kowalska, D. T. Yordanov, K. Blaum, P. Himpe, P. Lievens, S. Mallion, R. Neugart, G. Neyens, and N. Vermeulen, Phys. Rev. C **77**, 034307 (2008).

[27] D. T. Yordanov, M. L. Bissell, K. Blaum, M. De Rydt, Ch. Geppert, M. Kowalska, J. Krämer, K. Kreim, A. Krieger, P. Lievens, T. Neff, R. Neugart, G. Neyens, W. Nörtershäuser, R. Sánchez, and P. Vingerhoets, Phys. Rev. Lett. **108**, 042504 (2012).

[28] H. Schweickert, J. Dietrich, R. Neugart, and E. W. Otten, Nucl. Phys. A **246**, 187 (1975).

[29] N. Severijns, M. Tandecki, T. Phalet, and I. S. Towner, Phys. Rev. C **78**, 055501 (2008).

[30] E. Arimondo, M. Inguscio, and P. Violino, Rev. Mod. Phys. **49**, 31 (1977).

[31] S. Falke, E. Tiemann, C. Lisdat, H. Schnatz, and G. Grosche, Phys. Rev. A **74**, 032503 (2006).

[32] N. Bendali, H. T. Duong, and J. L. Vialle, J. Phys. B **14**, 4231 (1981).

[33] LBNL Isotopes Project Nuclear Data Dissemination home page, http://ie.lbl.gov/toi.html

[34] A.-M. Mårtensson-Pendrill, L. Pendrill, A. Salomonson, A. Ynnerman, and H. Warston, J. Phys. B **23**, 1749 (1990).

[35] H. D. Wohlfahrt, E. B. Shera, M. V. Hoehn, Y. Yamazaki, and R. M. Steffen, Phys. Rev. C **23**, 533 (1981).

[36] W. Bertozzi, J. Friar, J. Heisenberg, and J. Negele, Phys. Lett. B **41**, 408 (1972).

[37] B. A. Brown and A. Schwenk, Phys. Rev. C **89**, 011307 (2014).

[38] G. A. Lalazissis, T. Nikšić, D. Vretenar, and P. Ring, Phys. Rev. C **71**, 024312 (2005).

[39] S. Goriely (private communication).

[40] M. Sharma, G. Lalazissis, and P. Ring, Phys. Lett. B **317**, 9 (1993).

[41] I. Angeli and K. P. Marinova, At. Data Nucl. Data Tables **99**, 69 (2013).

[42] E. Caurier, K. Langanke, G. Martínez-Pinedo, F. Nowacki, and P. Vogel, Phys. Lett. B **522**, 240 (2001).

[43] B. A. Brown and W. D. M. Rae, Nucl. Data Sheets **120**, 115 (2014).

[44] Brookhaven National Laboratory, National Nuclear Data Center home page, http://www.nndc.bnl.gov

[45] R. A. Uher and R. A. Sorensen, Nucl. Phys. **86**, 1 (1966).

[46] H. Esbensen and G. F. Bertsch, Phys. Rev. C **28**, 355 (1983).

[47] J. Dobaczewski, P. Vogel, and A. Winther, Phys. Rev. C **29**, 1540 (1984).

[48] I. Angeli, Y. P. Gangrsky, K. P. Marinova, I. N. Boboshin, S. Y. Komarov, B. S. Ishkhanov, and V. V. Varlamov, J. Phys. G: Nucl. Part. Phys. **36**, 085102 (2009).

[49] R. A. Sorensen, Phys. Lett. **21**, 333 (1966).

[50] S. Goriely, Nucl. Phys. A **933**, 68 (2015).

[51] M. Avgoulea, Y. P. Gangrsky, K. P. Marinova, S. G. Zemlyanoi, S. Fritzsche, D. Iablonskyi, C. Barbieri, E. C. Simpson, P. D. Stevenson, J. Billowes, P. Campbell, B. Cheal, B. Tordoff, M. L. Bissell, D. H. Forest, M. D. Gardner, G. Tungate, J. Huikari, A. Nieminen, H. Penttilä, and J. Äystö, J. Phys. G: Nucl. Part. Phys. **38**, 025104 (2011).

[52] F. C. Charlwood, J. Billowes, P. Campbell, B. Cheal, T. Eronen, D. H. Forest, S. Fritzsche, M. Honma, A. Jokinen, I. D. Moore, H. Penttilä, R. Powis, A. Saastamoinen, G. Tungate, and J. Äystö, Phys. Lett. B **690**, 346 (2010).